GDCh

Research Articles

Angewandte
Chemie
International Edition
www.angewandte.org

Polymer Chemistry

On-Water Surface Synthesis of Vinylene-Linked Cationic Two-Dimensional Polymer Films as the Anion-Selective Electrode Coating

Ye Yang[+], Davood Sabaghi[+], Chang Liu[+], Arezoo Dianat, David Mücke, Haoyuan Qi,
Yannan Liu, Mike Hambsch, Zhi-Kang Xu, Minghao Yu,* Gianaurelio Cuniberti,
Stefan C. B. Mannsfeld, Ute Kaiser, Renhao Dong,* Zhiyong Wang,* and Xinliang Feng*

Abstract: Vinylene-linked two-dimensional polymers (V-2DPs) and their layer-stacked covalent organic frameworks (V-2D COFs) featuring high in-plane π-conjugation and robust frameworks have emerged as promising candidates for energy-related applications. However, current synthetic approaches are restricted to producing V-2D COF powders that lack processability, impeding their integration into devices, particularly within membrane technologies reliant upon thin films. Herein, we report the novel on-water surface synthesis of vinylene-linked cationic 2DPs films (**V-C2DP-1** and **V-C2DP-2**) via Knoevenagel polycondensation, which serve as the anion-selective electrode coating for highly-reversible and durable zinc-based dual-ion batteries (ZDIBs). Model reactions and theoretical modeling revealed the enhanced reactivity and reversibility of the Knoevenagel reaction on the water surface. On this basis, we demonstrated the on-water surface 2D polycondensation towards V-C2DPs films that show large lateral size, tunable thickness, and high chemical stability. Representatively, **V-C2DP-1** presents as a fully crystalline and face-on oriented film with in-plane lattice parameters of $a = b \approx 43.3$ Å. Profiting from its well-defined cationic sites, oriented 1D channels, and stable frameworks, **V-C2DP-1** film possesses superior bis(trifluoromethanesulfonyl)imide anion (TFSI⁻)-transport selectivity (transference, t_=0.85) for graphite cathode in high-voltage ZDIBs, thus triggering additional TFSI⁻-intercalation stage and promoting its specific capacity (from ~83 to 124 mAh g⁻¹) and cycling life (>1000 cycles, 95% capacity retention).

[*] Y. Yang,[+] D. Sabaghi,[+] Dr. H. Qi, Dr. Y. Liu, Dr. M. Yu, Prof. R. Dong,
Dr. Z. Wang, Prof. X. Feng
Center for Advancing Electronics Dresden & Faculty of Chemistry
and Food Chemistry, Technische Universität Dresden
01069 Dresden (Germany)
E-mail: minghao.yu@tu-dresden.de
        wang.zhiyong@tu-dresden.de
        xinliang.feng@tu-dresden.de

Dr. C. Liu,[+] Prof. Z.-K. Xu
MOE Engineering Research Center of Membrane and Water Treat-
ment, and Key Lab of Adsorption and Separation Materials &
Technologies of Zhejiang Province, Department of Polymer Science
and Engineering, Zhejiang University
310058 Hangzhou (China)

Dr. C. Liu,[+] Prof. Z.-K. Xu
The "Belt and Road" Sino-Portugal Joint Lab on Advanced
Materials, International Research Center for X Polymers, Zhejiang
University
310058 Hangzhou (China)

Dr. A. Dianat, Prof. G. Cuniberti
Institute for Materials Science and Max Bergmann Center for
Biomaterials, Technische Universität Dresden
01069 Dresden (Germany)

D. Mücke, Dr. H. Qi, Prof. U. Kaiser
Central Facility for Electron Microscopy, Electron Microscopy of
Materials Science, Universität Ulm
89081 Ulm (Germany)

Dr. C. Liu,[+] Dr. Z. Wang, Prof. X. Feng
Max Planck Institute of Microstructure Physics
06120 Halle (Germany)

Dr. M. Hambsch, Prof. S. C. B. Mannsfeld
Center for Advancing Electronics Dresden & Faculty of Electrical
and Computer Engineering, Technische Universität Dresden
01062 Dresden (Germany)

Prof. G. Cuniberti
Dresden Center for Computational Materials Science (DCMS),
Technische Universität Dresden
01062 Dresden (Germany)

Prof. R. Dong
Key Laboratory of Colloid and Interface Chemistry of the Ministry of
Education, School of Chemistry and Chemical Engineering,
Shandong University
250100 Jinan (China)
E-mail: renhaodong@sdu.edu.cn

[+] These authors contributed equally to this work.

Introduction

Two-dimensional polymers (2DPs) and their layer-stacked covalent organic frameworks (2D COFs) are an emerging class of highly ordered crystalline polymer materials.[1] Benefiting from their customizable structures and physico-chemical properties, 2DPs have exhibited great potential in electronics, optoelectronics, catalysis, energy storage and conversion.[2] Significant efforts have been devoted to the synthesis of crystalline 2DP thin films via interfacial synthesis methods,[3] yielding films characterized by extended regular π–π stacking structure and open straight channels. These attributes play a critical role in directing and maximizing the charge[4] and mass (e.g., gas molecule,[5] ions,[6] and organic molecules[7]) transport, making them appealing for the applications pertinent to ionic and molecular sieving membrane technologies.[8] Current 2DP thin films are typically constructed through dynamic covalent bonds (e.g., imine and boronate),[9] which enable an error-correction to make extended and well-ordered structures. Nonetheless, the inherent reversible nature of these bonds inevitably leads to poor chemical stability,[10] thereby imposing significant limitations on their practical applications, particularly in membrane technologies.

The construction of 2DPs utilizing irreversible bonds such as dioxin,[11] phenazine,[12] pyridinium[13] and C≡C (i.e. vinylene)[14] stands as a pivotal strategy in the pursuit of high chemical stability. Thus far, vinylene-linked 2DPs and 2D COFs (also called 2D polyarylene vinylene) have been mainly achieved through solvothermal synthetic methods of Knoevenagel,[15] aldol-type,[16] Horner–Wadsworth–Emmons (HWE)[17] and Wittig polycondensation.[18] In contrast to 2DPs connected by reversible linkages, V-2DPs exhibit extensive in-plane π-conjugation and robust frameworks.[19] However, despite intense progress being made in the synthesis and the exploration of their functionalities, V-2DPs are commonly produced as insoluble and unprocessable powders, presenting difficulties in their integration into devices that necessitate thin films.[20] The synthesis of crystalline and oriented V-2DP thin films is of paramount importance, yet remains a synthetic challenge.

In this work, we report the on-water surface synthesis of two novel vinylene-linked cationic 2DPs films (**V-C2DP-1** and **V-C2DP-2**) with oriented 1D channels and robust frameworks, which are demonstrated as desirable anion-selective electrode coating for zinc-based dual-ion batteries (ZDIBs). Through model reactions and theoretical calculations, we demonstrate the higher reactivity and reversibility of Knoevenagel reaction between 1,1′-bis(4-formylphenyl)-[4,4′-bipyridine]-1,1′-diium chloride (**1**) and phenylacetonitrile (**2**) as well as 1,1′-bis(4-(cyanomethyl)phenyl)-[4,4′-bipyridine]-1,1′-diium chloride (**4**) and benzaldehyde (**5**) on the water surface compared to the aqueous phase reaction. Building upon this insight, we successfully synthesize **V-C2DP-1** and **V-C2DP-2** with a large lateral size (~28 cm²), tunable thickness (~2–52 nm), and high chemical stability via the 2D polymerization of **1** and 2,2′,2″-(benzene-1,3,5-triyl)triacetonitrile (**7**), **4** and benzene-1,3,5-tricarbaldehyde (**8**), respectively. Utilizing aberration-corrected high-resolu-

tion transmission electron microscopy (AC-HRTEM) imaging and grazing-incidence wide-angle X-ray scattering (GI-WAXS), we identify the fully crystalline and face-on oriented feature of **V-C2DP-1**, displaying the hexagonal structure with in-plane lattice parameters of $a = b \approx 43.3$ Å. Taking advantage of its well-defined cationic sites, oriented 1D channels, and highly stable frameworks, **V-C2DP-1** exhibits superior bis(trifluoromethanesulfonyl)imide anion (TFSI⁻)-selective transport in promoting the operating voltage, intercalation stage, and reversibility of the graphite cathode in high-voltage ZDIBs. The resulting ZDIB exhibits significantly improved specific capacity (from ~83 to 124 mAh g⁻¹) and long-term cycling life (95 % capacity retention over 1000 cycles). These findings pave the way for developing novel V-2DP films boasting oriented 1D channels and highly stable frameworks, which offer a promising platform for advancing membranes in next-generation battery devices.

Results and Discussion

On-Water Surface Knoevenagel Condensation. To evaluate the feasibility of Knoevenagel polycondensation on the water surface, we conducted model reactions using two different sets of compounds, yielding 1,1′-bis(4-((Z)-2-cyano-2-phenylvinyl)phenyl)-[4,4′-bipyridine]-1,1′-diium (**3**) (**Model-I**, Scheme S1, Figure S1–4, Supporting Information) and 1,1′-bis(4-((Z)-1-cyano-2-phenylvinyl)phenyl)-[4,4′-bipyridine]-1,1′-diium (**6**) (**Model-II**, Scheme S2, Figure S5 and S6, Supporting Information), through the surfactant-monolayer assisted interfacial synthesis (SMAIS) method (Figure 1a, 1b and Scheme S3). In the model reactions, we followed a three-step procedure, as illustrated in Figure 1a. In Step I, sodium oleyl sulfate (SOS) monolayer was formed on the water surface in a crystallization dish (diameter, 6 cm). In Step II, 1 ml cesium carbonate (Cs₂CO₃, 15.3 μmol) aqueous solution of **1** (6.9 μmol) was added into the water phase. The increase in surface pressure and UV/Vis absorption intensity indicates the facilitated adsorption of **1** underneath the SOS monolayer, attributed to the electrostatic interaction between the pyridinium moieties and the anionic head groups of SOS (Figure S7 and S8). After 2 h, 1 ml aqueous solution of **2** (13.8 μmol) was injected into the water phase, and the system was kept at 50 °C under ambient conditions for 1 day (Step III). The time-evolving UV/Vis absorption of the product on the water surface shifts from 300 to 388 nm, revealing that **2** diffused to the adsorbed **1** and then initiated the Knoevenagel condensation (Figure S9). As a result, a macroscopic yellow film formed on the water surface. The identical synthetic procedure was performed for **Model-II**, yielding a yellow film as well.

The reaction pathway of **Model-I** is schematically elaborated in Supplementary Scheme 4. To assess the reactivity of Knoevenagel condensations, we employed matrix-assisted laser desorption ionization-time of flight mass spectrometry (MALDI-TOF MS) to analyze the resulting products obtained from the water surface and the
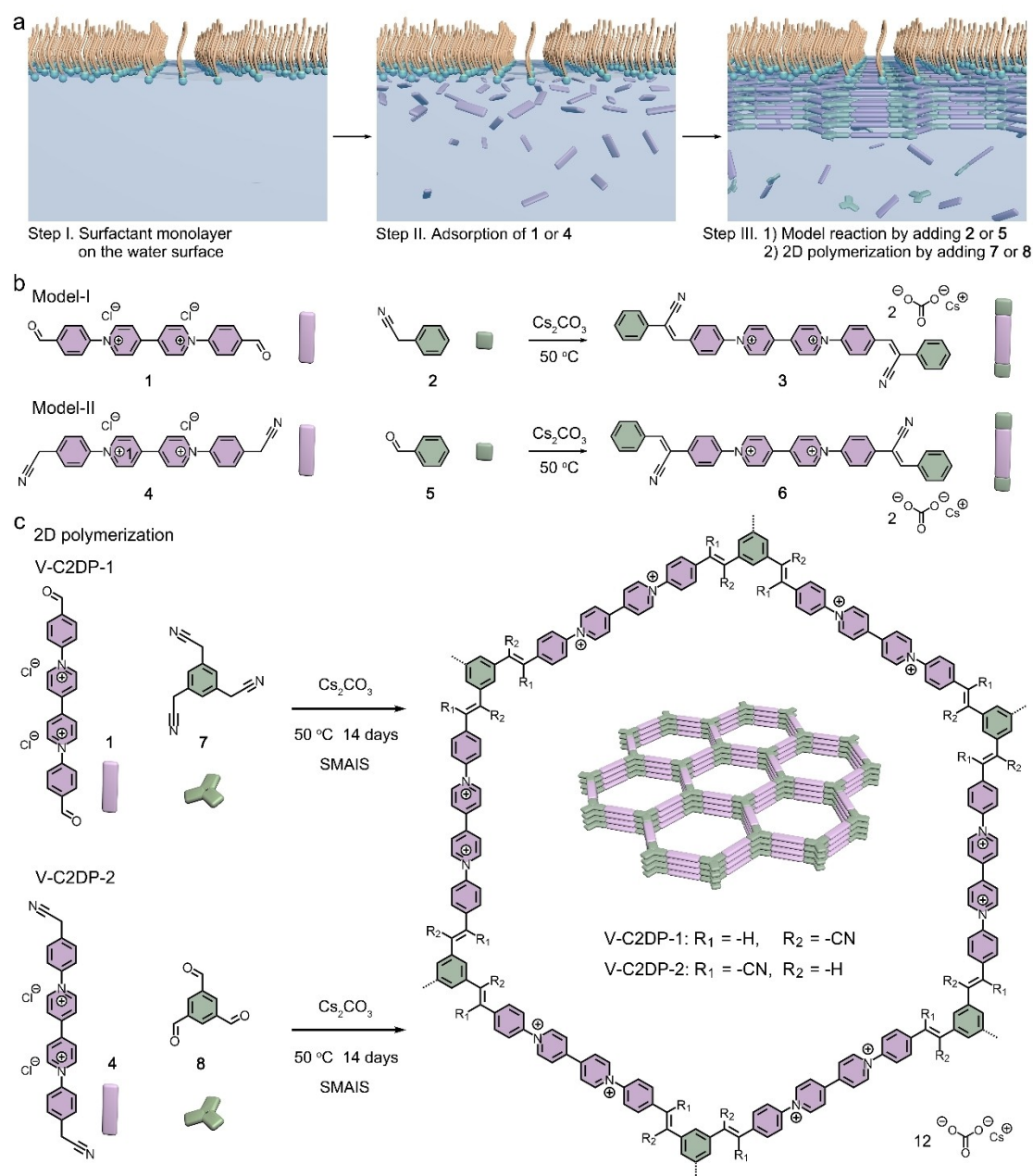
Figure 1. a) Schematic illustration of the synthetic procedure through the SMAIS method.[3a,13] b) Model reactions in the synthesis of **3** and **6**. c) A reaction Scheme illustrating the reaction of **1** with **7**, and **4** with **8** to form **V-C2DP-1** and **V-C2DP-2**, respectively.

aqueous solution. After 1 day of reaction, the MS spectrum of the product in the aqueous solution (Figure 2a, bottom) shows distinct peaks at $m/z = 366.1342$, $m/z = 465.1888$, $m/z = 483.2019$, $m/z = 582.2403$, and $m/z = 564.2285$, corresponding to the unreacted **1**, the intermediates **1a–c**, and final product **3**, respectively. In contrast, for the product on the water surface, only one peak of the final product **3** at $m/z = 564.2298$ was detected (Figure 2a, top), indicating a notably higher conversion rate of **3** on the water surface than in the aqueous solution. In addition, the MALDI-TOF MS of the **Model-II** products were also recorded to verify the universality of on-water surface Knoevenagel condensation (Figure 2b). In this case, a large proportion of **4** in the

aqueous solution remains unreacted, while the reaction occurs entirely on the water surface.

To gain deeper insights into the enhanced reactivity of Knoevenagel condensation on the water surface, we performed density functional theory (DFT) calculations to determine the reaction energy barriers on the water surface and in the aqueous solution (Figure 2c and S10). Notably, compared to that of in aqueous solution, the on-water surface synthesis demonstrates lower energy barriers for intermediates **2a** (−0.15 vs. 0.73 eV), **9a** (−0.66 vs. 1.80 eV), **9** (−0.57 vs. 0.87 eV), **9b** (0.29 vs. 1.16 eV), and compound **10** (−1.06 vs. −0.29 eV), respectively. This result underscores the significant impact of the 2D confinement
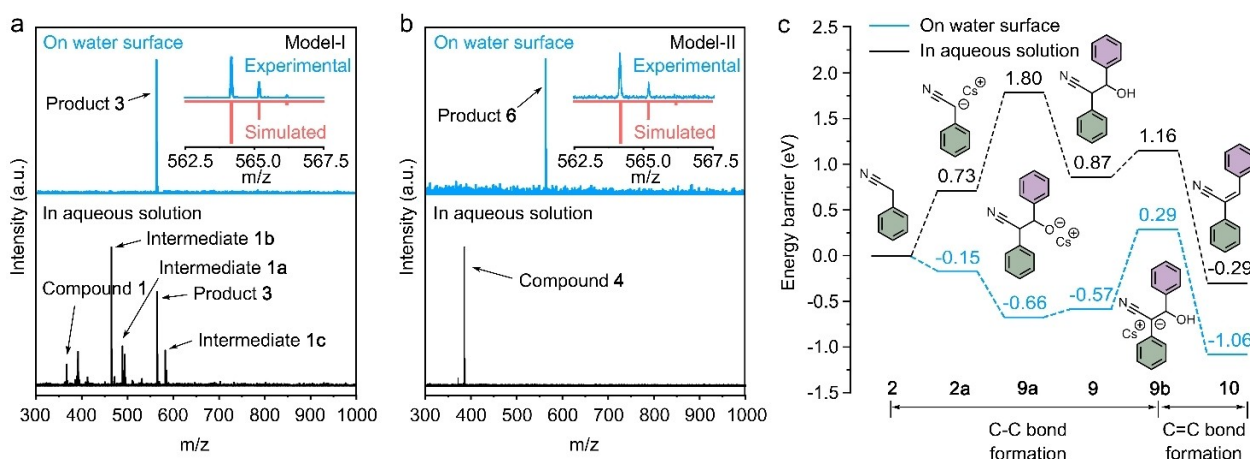
Figure 2. MALDI-TOF MS analysis of a) **Model-I** and b) **Model-II** reactions on the water surface (cyan) and in aqueous solution (black). c) Calculated energy profiles of the Knoevenagel reaction. The energies are with respect to **2**.

provided by the air/water interface, which effectively restrains the out-of-plane molecule movement and reduces steric hindrance. Particularly notable is the marked reduction in steric hindrance, notably exemplified in the nucleophilic attack of **2a** to **5** (Figure S11 and S12). This, in turn, greatly enhances the reactivity of the Knoevenagel reaction. Moreover, the energetic position of the **9a** on the water surface provides great possibilities for the C–C bond cleavage from **9** to **2** (activation energy $\triangle G = 0.57$ eV) in the reverse reaction compared to that in aqueous solution ($\triangle G = 0.93$ eV), suggesting higher reversibility of condensation on the water surface before the formation of the C=C (i.e. vinylene) bond.[19a] **Morphological and Structural Characterization of V-C2DPs**. Building upon the experimental and theoretical results of model reactions, we further executed the identical on-water surface synthesis of **V-C2DP-1** via (A$_2$+B$_3$)-type 2D polycondensation between **1** and 2,2′,2″-(benzene-1,3,5-triyl)triacetonitrile (**7**), yielding brilliant yellow films (Figure 1c and S13). The attenuated total reflection-Fourier transform infrared (ATR-FTIR) spectroscopy shows the appearance of C=C stretching (~1668 cm^{-1}) and R$_2$C=CHR vibration (~834 cm^{-1}), along with the disappearance of the C=O (~1741 cm^{-1}) and –CH$_2$– stretching vibration (~2938 cm^{-1}), indicating the complete conversion of the aldehyde group in **1** to the vinylene linkage in **V-C2DP-1** (Figure S14). Quantitative analysis of X-ray photoelectron spectroscopy (XPS) survey scan and its depth-profiling reveal the contents of C, N, O and Cs to be 74.9, 7.8, 13.2 and 4.1 atom%, respectively, consistent with the theoretical composition of **V-C2DP-1** (the C: N: O: Cs ratio of 17: 2: 3: 1) (Figure S15 and S16). The curve-fitted peaks at 285.6 eV (in XPS C 1s spectra), 400.6 eV and 402.6 eV (in XPS N 1s spectra) correspond to C–O (in CsCO$_3^-$), C≡N and N$^+$ (in **V-C2DP-1**), respectively (Figure S17 and S18), providing further evidence of the successful synthesis of **V-C2DP-1** film with CsCO$_3^-$ as counter ions.

The homogeneous morphology of **V-C2DP-1** films was illustrated by optical microscopy (OM) and scanning elec-

tron microscopy (SEM) (Figure S19). The **V-C2DP-1** film is observed to suspend freely over the square pores of a holey copper grid with a size of 30×30 μm^2 in the SEM images (Figure 3a), manifesting its high mechanical stiffness. The atomic force microscopy (AFM) images display an ultrasmooth surface for the as-prepared **V-C2DP-1** thin films with a thickness of ~52 nm and a root mean square (RMS) roughness of 0.19 nm in an area of 10×10 μm^2, respectively (Figure 3b). Note that the thickness of the obtained **V-C2DP-1** film can be finely tuned between ~2 and ~52 nm by changing the reaction time from 1 to 14 days (Figure S20 and S21).

To characterize the crystalline structure of V-C2DP-1, we conducted selected-area electron diffraction (SAED) and AC-HRTEM measurements on the obtained films. As shown in Figure 3c, the SAED pattern (bottom, inset) of **V-C2DP-1** displays an apparent diffraction ring with the nearest reflections at 0.45 nm^{-1} (d-spacing of ~22 Å), suggesting a polycrystalline nature. The AC-HRTEM image further reveals the homogeneous, fully crystalline structure with a well-ordered hexagonal lattice and a parameter of $a = b \approx 44$ Å, which is consistent with the simulated TEM image of the ABC-stacked **V-C2DP-1** derived by DFT method (bottom). The crystallization mechanism of **V-C2DP-1** was also monitored to demonstrate the critical role of surfactant-assisted water surface during the synthesis (Figure S22 and S23). To verify the detailed layer orientation and stacking mode of **V-C2DP-1** film on a macroscopic scale, we further conducted GIWAXS measurements. As shown in Figure 3d, we probed an intense arc at $Q_z = 1.85$ Å^{-1} in the out-of-plane direction, revealing a preferential face-on orientation of **V-C2DP-1** with an interlayer distance of 3.4 Å. The reflection peaks at $Q_{xy} = 0.29$ Å^{-1}, 0.52 Å^{-1}, 0.59 Å^{-1} and 0.79 Å^{-1} observed in the in-plane direction correspond to the (110), (030), (220) and (50) planes of **V-C2DP-1**, respectively. The in-plane intensity profile resolved in the GIWAXS pattern elucidates the hexagonal unit cell with $a = b = 43.3$ Å, $\gamma = 120°$, in agreement with an ABC stacking mode (Figure 3e and S24).
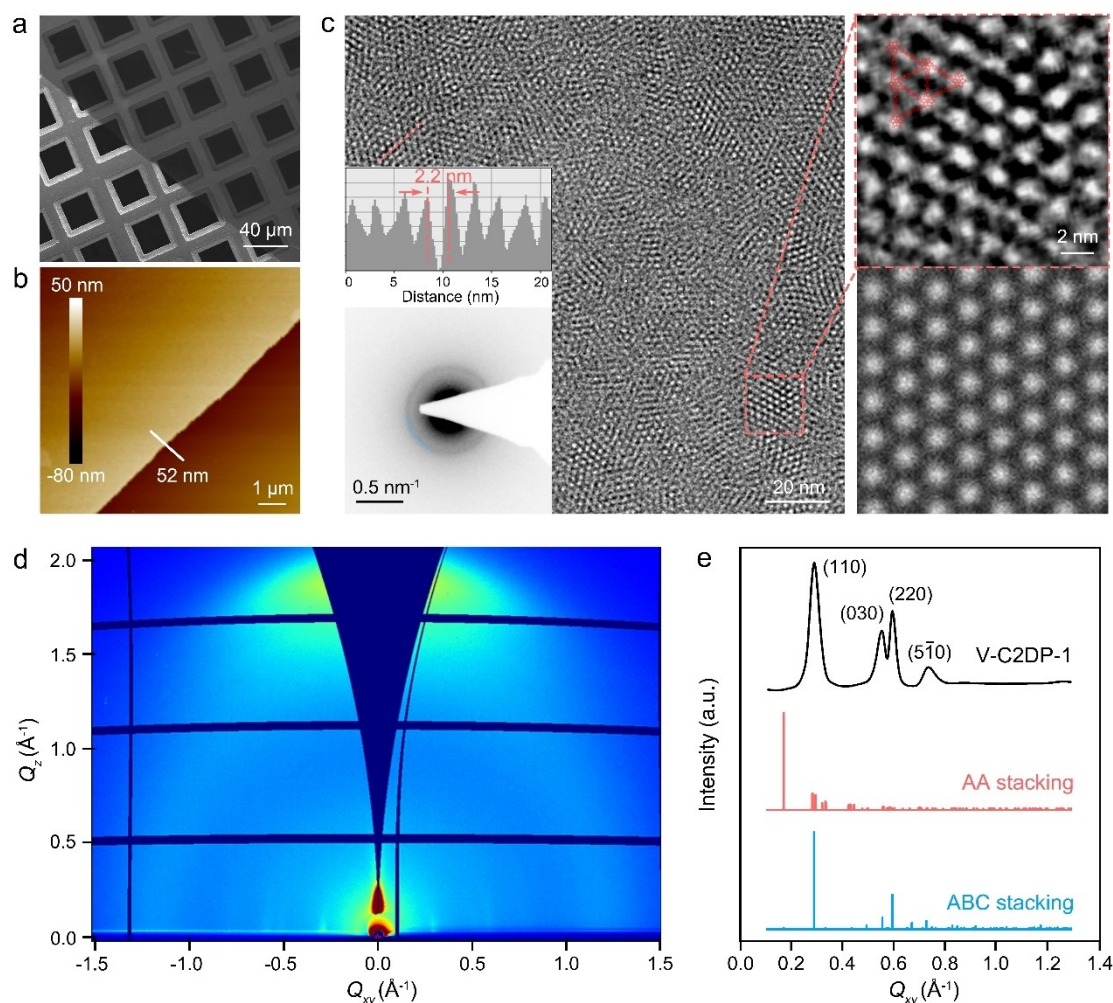
Figure 3. a) SEM image of **V-C2DP-1** on a copper grid with a hole area of ~900 μm². b) AFM image of **V-C2DP-1** on a SiO₂/Si substrate. The thicknesses of the films along the white line are marked. c) AC-HRTEM image of **V-C2DP-1**. Insert: Intensity profiles along the red line, SAED pattern, magnified (top right) and simulated (bottom right) AC-HRTEM images of **V-C2DP-1** with structure overlaid. d) GIWAXS pattern of **V-C2DP-1** film. e) Experimental and calculated in-plane (near $Q_z = 0$, Q represents scattering vector) projections.

Furthermore, we expanded the scope of the reaction to encompass the synthesis of **V-C2DP-2** by linking **4** and **8** under identical synthesis conditions (Figure S25). Leveraging the reaction for 14 days, we obtained **V-C2DP-2** film with a thickness of 26 nm and a RMS roughness of 0.22 nm in an area of 10×10 μm² (Figure S26). The chemical structure of the **V-C2DP-2** was confirmed through analysis of ATR-FTIR and XPS spectra (Figure S27–29). In addition, GI-WAXS measurement reveals a polycrystalline nature of **V-C2DP-2** with the ABC-stacked hexagonal lattice ($a = b = 46.8$ Å, $\gamma = 120°$), corresponding to the simulated crystal structure (Figure S30 and S31). This observation underscores the generality of the Knoevenagel reaction in the synthesis of V-C2DP thin films on the water surface.

Interfacial Coating of Graphite Cathodes in ZDIBs. ZDIBs as promising candidates for large-scale energy storage, have attracted growing interest.[21] Nonaqueous electrolytes in rechargeable ZDIBs provide an option to increase the working voltage and energy density further. However, previous studies on carbonate-based electrolytes

have encountered severe electrolyte oxidation problems,[22] which constrain the option of high-voltage cathode materials for nonaqueous ZDIBs. Compared to **V-C2DP-2**, the **V-C2DP-1** film exhibits a higher crystallinity and face-on oriented structure, thereby providing an efficient and short pathway for ion transport. The presence of cationic sites (i.e. viologen moieties) endows the **V-C2DP-1** film with a high surface Zeta potential of 66.8 mV at pH ~7 (Figure S32), which is anticipated to afford outstanding selectivity and conductivity of anion transport.[23] In addition, the robust vinylene linkage imparts **V-C2DP-1** with excellent chemical stability, even in strongly acidic, alkaline, as well as organic solvents (Figure S33–S35, Table S1),[24] making it a promising protective coating for high-voltage ZDIB. To examine the effect of **V-C2DP-1** film overlaid on graphite cathodes (**G/V-C2DP-1**), we constructed ZDIB devices with a Zn foil as the anode, pristine graphite or **G/V-C2DP-1** as the cathode, and 2 M Zn(TFSI)₂ dissolved in dimethyl carbonate (DMC) as the electrolyte (Figure 4a). **V-C2DP-1** as a homogeneous coating was tightly attached to the surface of
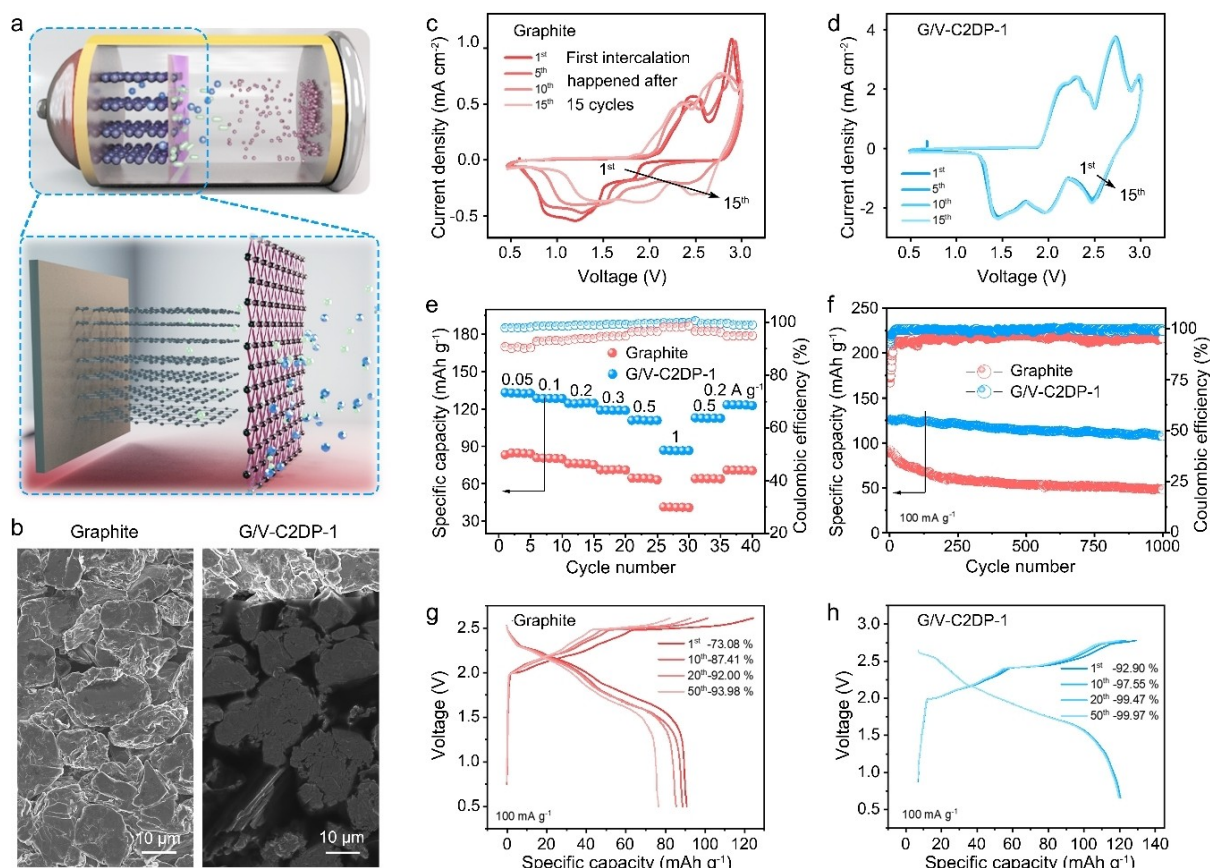
Figure 4. a) Schematic illustration showing the functions of **V-C2DP-1** as the electrode skin in promoting the anion-intercalation chemistries. b) SEM images of graphite and **V-C2DP-1** coated graphite electrodes. CV curves of c) graphite and d) **G/V-C2DP-1** cathodes at 1 mV s^{-1}. e) Cyclic performance of the graphite and **G/V-C2DP-1** at 100 mA g^{-1}. f) Rate performance of the graphite and **G/V-C2DP-1** electrodes. GCD curves of g) graphite and h) **G/V-C2DP-1** at 100 mA g^{-1}.

the graphite cathode (Figure 4b). The cyclic voltammetry (CV) curves of graphite (Figure 4c) and **G/V-C2DP-1** (Figure 4d) both show several pairs of redox peaks in the voltage range of 0.50–2.85 V (vs. Zn), corresponding to different TFSI$^-$ intercalation/deintercalation stages of graphite (Figure 4c and 4d).[25] Graphite cathodes exhibit an inconsistent CV pattern upon initial cycles, while the CV curves of **G/V-C2DP-1** cathodes remain constant, demonstrating the irreversible electrolyte oxidation process without protective **V-C2DP-1** film.

We also recorded the charge–discharge profiles of graphite and **G/V-C2DP-1** at 100 mA g^{-1} by gradually increasing the operating voltage (Figure S36). The maximum voltage for the graphite electrode was limited to 2.6 V due to parasitic electrolyte decomposition on the graphite cathode. In contrast, **V-C2DP-1** effectively isolates the electrode from contacting electrolyte, empowering **G/V-C2DP-1** with robust resistance towards electrolyte decomposition with a maximum voltage of 2.85 V. More importantly, with the high operating voltage, **G/V-C2DP-1** was able to achieve an additional TFSI$^-$-intercalation (deintercalation) stage,[25] which affords a substantially enhanced specific capacity of 124 mAh g^{-1} compared with graphite (83 mAh g^{-1}) at 100 mA g^{-1} (Figure 4e). Consequently, the ZDIB device

with the **G/V-C2DP-1** cathode provides a high energy density of 77 Wh kg^{-1}, while the device with the graphite cathode only reaches 27 Wh kg^{-1} (Figure S37). Even at a large current density of 1 A g^{-1}, **G/V-C2DP-1** still delivers a high specific capacity of 96 mAh g^{-1}, significantly exceeding graphite (43 mAh g^{-1}).

Next, an evaluation of the long-term cycling stability was conducted for both graphite and **G/V-C2DP-1**, each subjected to a current density of 100 mA g^{-1} and utilizing distinct voltage windows of 0.5–2.6 V and 0.5–2.85 V, respectively (Figure 4f). After 1,000 cycles, the specific capacity of **G/V-C2DP-1** decays from 124.0 mAh g^{-1} to 117.8 mAh g^{-1}, referring to outstanding capacity retention of 95 %. After the cycling test, the **V-C2DP-1** coating effectively preserved its chemical and crystalline structure (Figure S38 and S39). By contrast, fast capacity decay was observed for graphite with a specific capacity dropped from 83.1 mAh g^{-1} to 54.2 mAh g^{-1} after 250 cycles. To understand the differentiated cycling performance, we derived the 1st, 10th, 20th, and 50th charge/discharge profiles of graphite (Figure 4g) and **G/V-C2DP-1** (Figure 4h). Notably, **G/V-C2DP-1** exhibits a high initial coulombic efficiency of 92.90 % in spite of its higher operating voltage, while the initial coulombic efficiency of graphite can only reach

73.08%. At the 50th cycle, **G/V-C2DP-1** achieved an ideal coulombic efficiency of 99.97%, indicating superior TFSI⁻-intercalation/deintercalation reversibility. Compared to that of **G/V-C2DP-1**, graphite can only reach a coulombic efficiency of 93.98% at the 50th cycle. These results reveal the pivotal contribution of the **V-C2DP-1** coating in promoting the reversibility and durability of the graphite cathode.

To elucidate the underlying role of V-C2DP-1 in ZDIB, we further investigated the ion-selective transport performance through transference number measurement and molecular dynamic (MD) calculation. As expected, electrostatic potential (ESP) surface calculation presents positively-charged triangular channels in **V-C2DP-1**, contributing to the anion-selective transport of electrolyte (Figure 5a). The energy barrier for solvated Zn^{2+} and TFSI⁻ ions in the out-of-plane path of **V-C2DP-1** in DMC was calculated to assess ion transport ability through these 1D channels. Despite the smaller size of the Zn^{2+} ion, the diffusion barrier (187 kJ mol⁻¹) is higher than that of the TFSI⁻ ion (−55 kJ mol⁻¹), indicating the lower transport ability of the Zn^{2+} ion in the channels arising from the electrostatic repulsion (Figure 5b). To validate this observation, the TFSI⁻ transference number (t_) through PP/**V-C2DP-1** was calculated using Bruce-Vincent equations. PP/**V-C2DP-1**

film possesses a much higher t_ (0.85) than the control sample (PP, 0.44), demonstrating the superior TFSI⁻ selectivity of **V-C2DP-1** film (Figure 5c). MD simulation was also performed to visualize this process (Video S1 and S2). The MD snapshot at 500 ns shows the direct contact and intercalation between the graphite electrode and both solvated Zn^{2+} and TFSI⁻ ions, resulting in irreversible structural distortion of graphite and the formation of a dense electrolyte decomposition layer on the electrode (Figure 5d and 5e). The electrolyte decomposition causes the impedance of the graphite cathode to increase, which can be identified by the impedance spectroscopy (Figure S40). The collected Nyquist plots were analyzed with the equivalent circuit, and the fitting result is shown in Table S2. After 5 charge/discharge cycles, such thick decomposition layer drastically increases the interphase resistance (R_{CEI}) and charge-transfer resistance (R_{ct}) of graphite from 3.4 and 48.3 Ω to 23.5 and 72.3 Ω, respectively. In contrast, the R_{CEI} of the **G/V-C2DP-1** electrode increased slightly from 7.7 Ω to 10.3 Ω after 5 charge/discharge cycles. The **G/V-C2DP-1** electrode before cycling showed a higher R_{ct} (68.6 Ω) than the graphite electrode due to the to-be-activated TFSI⁻-wettability of **V-C2DP-1** film. **V-C2DP-1** film effectively blocks the intercalation of solvated Zn^{2+} while allowing the efficient transport of TFSI⁻ ions, enabling the graphite
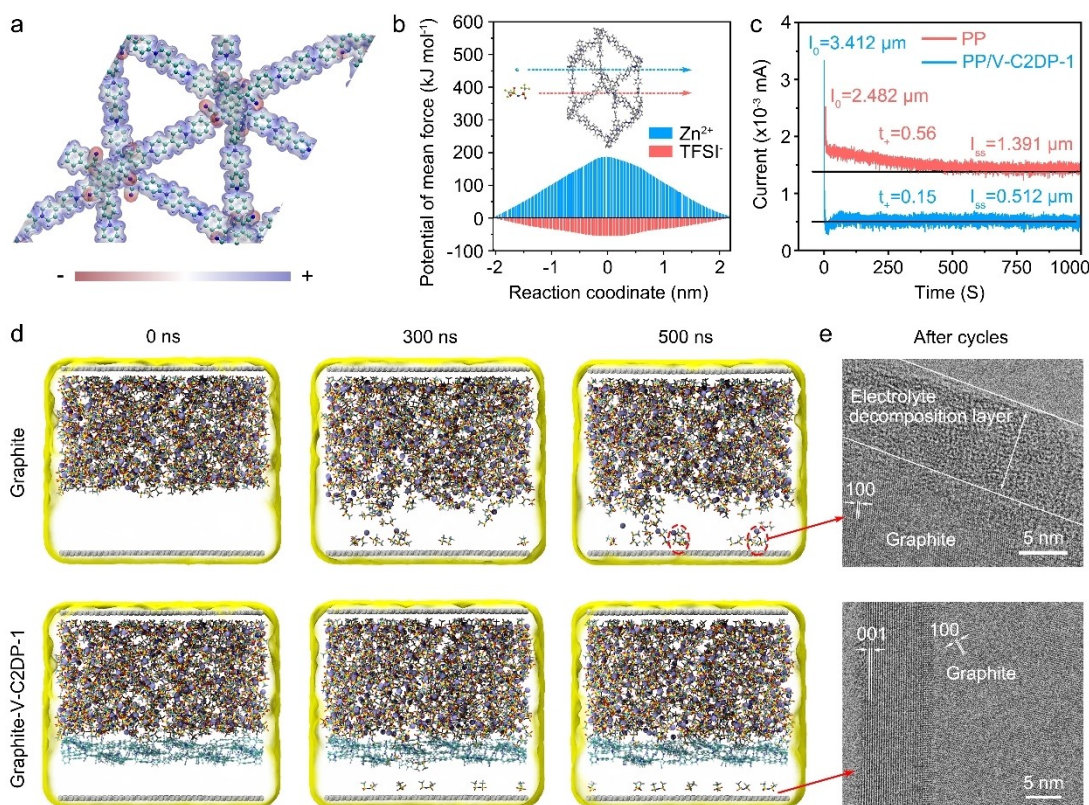

Figure 5. a) ESP plots of **V-C2DP-1** (isosurface value = 0.01 e Å⁻³). The blue and red colors denote deficient and rich electron density, respectively. b) Zn^{2+} and TFSI⁻-diffusion energy barriers. c) Chronoamperometry profiles of polypropylene (PP) (control) and **V-C2DP-1** on PP (PP/**V-C2DP-1**) in symmetric Zn//Zn Swagelok cells with a step potential of 10 mV. I_0 and I_{SS} represent the current at the beginning state and steady state, respectively. d) Representative MD simulation snapshots of graphite and **G/V-C2DP-1** at 0, 300 and 500 ns. e) TEM images of the graphite grain in graphite and **G/V-C2DP-1** electrode after 20 GCD cycles.

electrode to maintain its original layered structure and suppressing the decomposition at higher voltage (Figure S41). Meanwhile, the R_{ct} of **G/V-C2DP-1** after 5-cycle activation reduces to 53.2 Ω, approaching the original R_{ct} of the graphite electrode. These results support that the **V-C2DP-1** film can effectively prevent the formation of the dense electrolyte decomposition layer, leading to an improvement in charge-storage capacity and the lifetime of the graphite cathode.

Conclusions

In summary, we have demonstrated the on-water surface synthesis of novel cationic V-2DP films based on the enhanced reactivity and reversibility of the Knoevenagel reaction in comparison to its occurrence in an aqueous solution, as evidenced by the model reactions and modeling analysis. Two crystalline **V-C2DP-1** and **V-C2DP-2** films, characterized by a large area, tunable thickness, and high chemical stability, were achieved. In particular, **V-C2DP-1** possessed the fully crystalline and face-on oriented structure with in-plane lattice parameters of $a = b \approx 43.3$ Å. Profiting from its well-defined cationic sites, oriented 1D channels, and robust frameworks, the **V-C2DP-1** film exhibited superior anion-selective transport, which contributes to promoting the operating voltage, intercalation stage, and reversibility of the graphite cathode in high-voltage ZDIB. This work sheds light on the development of highly oriented and highly stable V-2DP films and bears significant potential in advancing next-generation energy devices.

Acknowledgements

Conflict of Interest

The authors declare no conflict of interest.

Data Availability Statement

The data that support the findings of this study are available from the corresponding author upon reasonable request.

Keywords: Interfacial Chemistry · Vinylene-Linked 2DP Films · Selective Ion Transport · Electrode Coating · Dual-Ion Batteries

[1] a) C. S. Diercks, O. M. Yaghi, *Science* **2017**, *355*, eaal1585; b) N. Huang, P. Wang, D. Jiang, *Nat. Rev. Mater.* **2016**, *1*, 16068; c) J. W. Colson, W. R. Dichtel, *Nat. Chem.* **2013**, *5*, 453–465; d) X. Li, P. Yadav, K. P. Loh, *Chem. Soc. Rev.* **2020**, *49*, 4835–4866; e) C. Wang, Z. Zhang, Y. Zhu, C. Yang, J. Wu, W. Hu, *Adv. Mater.* **2022**, *34*, 2102290.

[2] a) Q. Zhang, S. Dong, P. Shao, Y. Zhu, Z. Mu, D. Sheng, T. Zhang, X. Jiang, R. Shao, Z. Ren, J. Xie, X. Feng, B. Wang, *Science* **2022**, *378*, 181–186; b) F. Yang, S. Cheng, X. Zhang, X. Ren, R. Li, H. Dong, W. Hu, *Adv. Mater.* **2018**, *30*, 1702415; c) S. Lin, C. S. Diercks, Y.-B. Zhang, N. Kornienko, E. M. Nichols, Y. Zhao, A. R. Paris, D. Kim, P. Yang, O. M. Yaghi, C. J. Chang, *Science* **2015**, *349*, 1208–1213; d) N. Keller, T. Bein, *Chem. Soc. Rev.* **2021**, *50*, 1813–1845.

[3] a) K. Liu, H. Qi, R. Dong, R. Shivhare, M. Addicoat, T. Zhang, H. Sahabudeen, T. Heine, S. Mannsfeld, U. Kaiser, Z. Zheng, X. Feng, *Nat. Chem.* **2019**, *11*, 994–1000; b) H. Qi, H. Sahabudeen, B. Liang, M. Položij, M. A. Addicoat, T. E. Gorelik, M. Hambsch, M. Mundszinger, S. Park, B. V. Lotsch, S. C. B. Mannsfeld, Z. Zheng, R. Dong, T. Heine, X. Feng, U. Kaiser, *Sci. Adv.* **2020**, *6*, eabb5976.

[4] a) C. Jiang, M. Tang, S. Zhu, J. Zhang, Y. Wu, Y. Chen, C. Xia, C. Wang, W. Hu, *Angew. Chem. Int. Ed.* **2018**, *57*, 16072–16076; b) C. Yang, K. Jiang, Q. Zheng, X. Li, H. Mao, W. Zhong, C. Chen, B. Sun, H. Zheng, X. Zhuang, J. A. Reimer, Y. Liu, J. Zhang, *J. Am. Chem. Soc.* **2021**, *143*, 17701–17707.

[5] A. a. Knebel, J. Caro, *Nat. Nanotechnol.* **2022**, *17*, 911–923.

[6] Y. Li, Q. Wu, X. Guo, M. Zhang, B. Chen, G. Wei, X. Li, X. Li, S. Li, L. Ma, *Nat. Commun.* **2020**, *11*, 599.

[7] K. Dey, M. Pal, K. C. Rout, S. Kunjattu, H. A. Das, R. Mukherjee, U. K. Kharul, R. Banerjee, *J. Am. Chem. Soc.* **2017**, *139*, 13083–13091.

[8] a) H. Fan, M. Peng, I. Strauss, A. Mundstock, H. Meng, J. Caro, *Nat. Commun.* **2021**, *12*, 38; b) S. Wang, L. Yang, G. He, B. Shi, Y. Li, H. Wu, R. Zhang, S. Nunes, Z. Jiang, *Chem. Soc. Rev.* **2020**, *49*, 1071–1089.

[9] a) L. Ascherl, E. W. Evans, M. Hennemann, D. Di Nuzzo, A. G. Hufnagel, M. Beetz, R. H. Friend, T. Clark, T. Bein, F. Auras, *Nat. Commun.* **2018**, *9*, 3802; b) A. M. Evans, A. Giri,

V. K. Sangwan, S. Xun, M. Bartnof, C. G. Torres-Castanedo, H. B. Balch, M. S. Rahn, N. P. Bradshaw, E. Vitaku, D. W. Burke, H. Li, M. J. Bedzyk, F. Wang, J.-L. Brédas, J. A. Malen, A. J. H. McGaughey, M. C. Hersam, W. R. Dichtel, P. E. Hopkins, *Nat. Mater.* **2021**, *20*, 1142–1148; c) H. Sahabudeen, H. Qi, B. A. Glatz, D. Tranca, R. Dong, Y. Hou, T. Zhang, C. Kuttner, T. Lehnert, G. Seifert, U. Kaiser, A. Fery, Z. Zheng, X. Feng, *Nat. Commun.* **2016**, *7*, 13461.

[10] F. Haase, B. V. Lotsch, *Chem. Soc. Rev.* **2020**, *49*, 8469–8500.

[11] B. Zhang, M. Wei, H. Mao, X. Pei, S. A. Alshmimri, J. A. Reimer, O. M. Yaghi, *J. Am. Chem. Soc.* **2018**, *140*, 12715–12719.

[12] E. Vitaku, C. N. Gannett, K. L. Carpenter, L. Shen, H. D. Abruña, W. R. Dichtel, *J. Am. Chem. Soc.* **2019**, *142*, 16–20.

[13] Z. Wang, Z. Zhang, H. Qi, A. Ortega-Guerrero, L. Wang, K. Xu, M. Wang, S. Park, F. Hennersdorf, A. Dianat, A. Croy, H. Komber, G. Cuniberti, J. J. Weigand, U. Kaiser, R. Dong, X. Feng, *Nat. Synth.* **2022**, *1*, 69–76.

[14] E. Jin, J. Li, K. Geng, Q. Jiang, H. Xu, Q. Xu, D. Jiang, *Nat. Commun.* **2018**, *9*, 4143.

[15] a) E. Jin, M. Asada, Q. Xu, S. Dalapati, M. A. Addicoat, M. A. Brady, H. Xu, T. Nakamura, T. Heine, Q. Chen, D. Jiang, *Science* **2017**, *357*, 673–676; b) X. Zhuang, W. Zhao, F. Zhang, Y. Cao, F. Liu, S. Bi, X. Feng, *Polym. Chem.* **2016**, *7*, 4176–4181.

[16] a) A. Acharjya, P. Pachfule, J. Roeser, F. J. Schmitt, A. Thomas, *Angew. Chem. Int. Ed.* **2019**, *58*, 14865–14870; b) Z. Wang, Y. Yang, Z. Zhao, P. Zhang, Y. Zhang, J. Liu, S. Ma, P. Cheng, Y. Chen, Z. Zhang, *Nat. Commun.* **2021**, *12*, 1982.

[17] D. L. Pastoetter, S. Xu, M. Borrelli, M. Addicoat, B. P. Biswal, S. Paasch, A. Dianat, H. Thomas, R. Berger, S. Reineke, E. Brunner, G. Cuniberti, M. Richter, X. Feng, *Angew. Chem. Int. Ed.* **2020**, *59*, 23620–23625.

[18] Y. Liu, S. Fu, D. L. Pastoetter, A. H. Khan, Y. Zhang, A. Dianat, S. Xu, Z. Liao, M. Richter, M. Yu, M. Položij, E. Brunner, G. Cuniberti, T. Heine, M. Bonn, H. I. Wang, X. Feng, *Angew. Chem. Int. Ed.* **2022**, *134*, e202209762.

[19] a) D. Becker, B. P. Biswal, P. Kalen̨czuk, N. Chandrasekhar, L. Giebeler, M. Addicoat, S. Paasch, E. Brunner, K. Leo, A. Dianat, G. Cuniberti, R. Berger, X. Feng, *Chem. Eur. J.* **2019**, *25*, 6562–6568; b) H. Yu, D. Wang, *J. Am. Chem. Soc.* **2020**, *142*, 11013–11021; c) R. Chen, J. L. Shi, Y. Ma, G. Lin, X. Lang, C. Wang, *Angew. Chem. Int. Ed.* **2019**, *58*, 6430–6434; d) S. Xu, G. Wang, B. P. Biswal, M. Addicoat, S. Paasch, W. Sheng, X. Zhuang, E. Brunner, T. Heine, R. Berger, X. Feng, *Angew. Chem. Int. Ed.* **2019**, *131*, 859–863.

[20] a) S. Bi, C. Yang, W. Zhang, J. Xu, L. Liu, D. Wu, X. Wang, Y. Han, Q. Liang, F. Zhang, *Nat. Commun.* **2019**, *10*, 2467; b) L. Cao, I.-C. Chen, C. Chen, D. B. Shinde, X. Liu, Z. Li, Z. Zhou, Y. Zhang, Y. Han, Z. Lai, *J. Am. Chem. Soc.* **2022**, *144*, 12400–12409.

[21] L. Wang, M. Peng, J. Chen, X. Tang, L. Li, T. Hu, K. Yuan, Y. Chen, *ACS Nano* **2022**, *16*, 2877–2888.

[22] a) E. Krämer, T. Schedlbauer, B. Hoffmann, L. Terborg, S. Nowak, H. J. Gores, S. Passerini, M. Winter, *J. Electrochem. Soc.* **2012**, *160*, A356; b) A. Heckmann, M. Krott, B. Streipert, S. Uhlenbruck, M. Winter, T. Placke, *ChemPhysChem* **2017**, *18*, 156–163.

[23] a) D. Sabaghi, Z. Wang, P. Bhauriyal, Q. Lu, A. Morag, D. Mikhailovia, P. Hashemi, D. Li, C. Neumann, Z. Liao, A. M. Dominic, A. S. Nia, R. Dong, E. Zschech, A. Turchanin, T. Heine, M. Yu, X. Feng, *Nat. Commun.* **2023**, *14*, 760; b) Z. Huang, M. Fang, B. Tu, J. Yang, Z. Yan, H. G. Alemayehu, Z. Tang, L. Li, *ACS Nano* **2022**, *16*, 17149–17156; c) M. Wang, P. Zhang, X. Liang, J. Zhao, Y. Liu, Y. Cao, H. Wang, Y. Chen, Z. Zhang, F. Pan, Z. Zhang, Z. Jiang, *Nat. Sustain.* **2022**, *5*, 518–526.

[24] P. J. Stephens, F. J. Devlin, C. F. Chabalowski, M. J. Frisch, *J. Phys. Chem.* **1994**, *98*, 11623–11627.

[25] G. Wang, M. Zhu, G. Chen, Z. Qu, B. Kohn, U. Scheler, X. Chu, Y. Fu, O. G. Schmidt, X. Feng, *Adv. Mater.* **2022**, *34*, 2201957.

Research Articles

Polymer Chemistry

Y. Yang, D. Sabaghi, C. Liu, A. Dianat,
D. Mücke, H. Qi, Y. Liu, M. Hambsch, Z.-
K. Xu, M. Yu,* G. Cuniberti,
S. C. B. Mannsfeld, U. Kaiser, R. Dong,*
Z. Wang,* X. Feng* ———— **e202316299**

On-Water Surface Synthesis of Vinylene-Linked Cationic Two-Dimensional Polymer Films as the Anion-Selective Electrode Coating

V-C2DP-1: $R_1 = -H$, $R_2 = -CN$
V-C2DP-2: $R_1 = -CN$, $R_2 = -H$
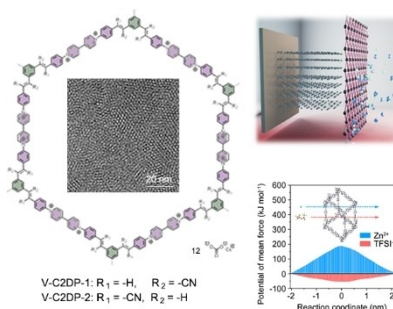
Two vinylene-linked cationic 2DPs (V-C2DPs) are synthesized on the water surface via Knoevenagel reaction, presenting as fully crystalline and highly oriented thin films. The obtained V-C2DPs exhibit well-defined cationic sites and 1D channels, facilitating the anion-selective transport. The integration of V-C2DPs as graphite cathode coatings into zinc-based dual-ion batteries (ZDIBs) enables to improve its specific capacity and cycling life.